

# Inflow Modeling of a Rotor in Hover and Forward Flight Using Potential Flow approach

Basit Ali

Department of Aeronautics and Astronautics,  
Institute of Space Technology, Islamabad, Pakistan  
[basitali2784@gmail.com](mailto:basitali2784@gmail.com)

**Abstract**— The paper presents a comparative study of the various inflow models for a rotor blade in hover and forward flight case based on potential flow analysis. The classical actuator disk approach suggests a uniform inflow distribution but when coupled with Blade Element Theory (BET) and Momentum Theory (MT) combined as Blade Element Momentum Theory (BEMT) gives accurate prediction of inflow distribution in hover state which is symmetric about the axis of rotation. Landgrebe’s prescribed wake model is used to determine the effect of tip vortex and the vortex sheet below the rotor plane in hovering flight. In forward flight, the wake interactions become more complex and the inflow distribution becomes more asymmetric. Linear inflow models including Drees’, Payne’s, Pit and Peter’s models are employed for longitudinal and lateral inflow distribution. Mangler and Squire’s (MNS) model is finally implemented to see the effect of superposition of Type-I and Type-III loadings on the rotor. The results of each model are compared with the experimental results for verification. BEMT gives most accurate prediction of inflow distribution in hover while MNS model gives best results in forward flight.

**Keywords**—rotor; inflow distribution; hover; forward flight; vortex; potential flow

## I. INTRODUCTION

A typical rotorcraft utilizes aerodynamic loads on its blades for both lift and thrust force. The propulsive performance of the rotor blades is hence a direct indicative of the flight performance of a rotorcraft. A rotorcraft has either a single main rotor with a tail rotor which forms the more conventional helicopter design, or it may have two rotors in coaxial configuration. More recently multi-copter concepts are being designed including quad-copters, hexa-copters and octa-copters. Each of these designs uses a number of rotor blades which force the air above the rotor disk plane to accelerate while passing through the rotor, more like sucking the air, resulting in the induced velocity distribution over the disk also called inflow. As opposed to fixed wing aircrafts, the incident velocity over each airfoil section along the radius of the disk is not constant but it varies linearly with the radial position. This variation in incident velocity coupled with the induced velocity gives the resultant velocity field as seen by each blade section.

$$V_{hover}(r) = r.\omega + V_i \quad (1)$$

This distribution of velocity then gives the blade loadings including thrust and moment. The normal modes of operation of any rotorcraft include hover, climbing and descending flight and forward flight cases. In hover flight, as seen in figure 1.a,

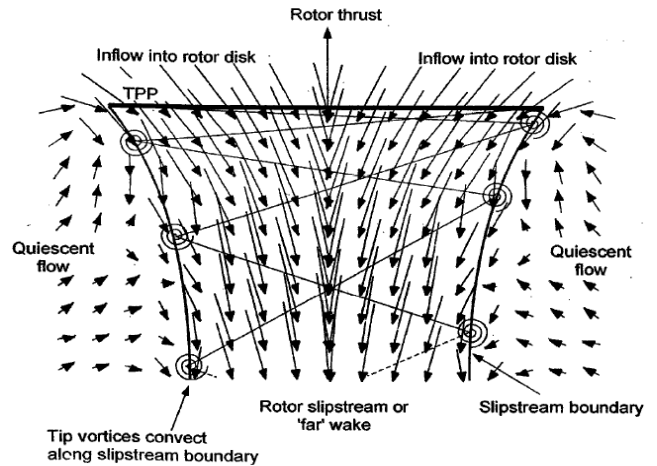
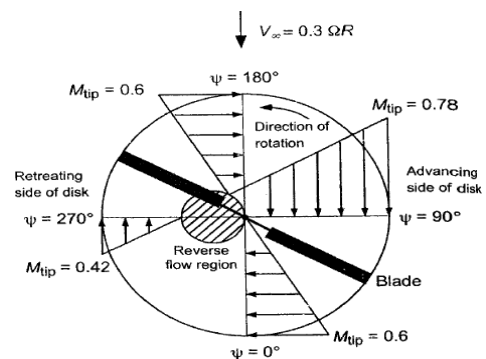


Fig 1.a Velocity field of a 2-bladed rotor in hover [5]

the velocity distribution is symmetric about the axis of rotation of the rotor and so is the blade loading. In forward flight case, the situation is no more symmetric and the blades experience forces which are a function of the azimuth or blade position along the disk. This makes the inflow modeling difficult because of the dynamics of the blade resulting from the imbalanced forces over the disk making the flat rotor disk into a cone because of flapping motion of blades which is periodic in nature. A part of the blade which is advancing towards the flight direction, experiences higher velocity while the other part which is retreating experiences lower velocity. All other blade components experience a component of the free stream velocity  $V_\infty$ . The resultant velocity in forward flight is

$$V_{forward}(r, \omega) = r.\omega + V_i + V_\infty \sin \psi \quad (2)$$



**Fig 1.b** In plane incident velocity distribution in forward flight [5]

## II. POTENTIAL FLOW THEORY

Potential flow theory is widely used in fluid dynamics to simplify the computations involved by making 3 key assumptions as follows

- (i) Flow is incompressible. This is valid for low speed operation and finds application in most commercial micro and nano scale rotorcrafts and wind turbines. This assumption is mathematically employed through the continuity equation which simplifies to

$$\nabla \cdot \mathbf{V} = 0 \quad (3)$$

- (ii) Flow is Irrotational. This is to say that viscous forces are dominant over a thin boundary layer and flow is Irrotational throughout the rest of flow field. This is employed mathematically setting the vorticity to 0.

$$\nabla \times \mathbf{V} = 0 \quad (4)$$

- (iii) Flow is inviscid. This is applicable in high Reynolds number flows where inertial forces are more dominant.

In potential flow approach velocity is often defined in terms of velocity potential  $\phi$  as

$$\mathbf{V} = \nabla \phi \quad (5)$$

The combined results of (4) and (5) give the Laplace equation which is applicable on potential flow making the superposition easier which has been employed in the later part of this paper in MnS model.

$$\nabla^2 \phi = 0 \quad (6)$$

## III. HOVER INFLOW DISTRIBUTION

### A. Actuator Disk Approach and Momentum Theory

The rotor blade produces upward thrust in hover by driving the air column in downwards direction through the rotor plane. The laws of mass, momentum and energy can be used to calculate the upward thrust as a function of induced velocity. This approach is commonly referred to as the momentum theory. This theory assumes the rotor blade as an actuator disk across which there is a sudden change in pressure which generates upward thrust. The air column passing through the actuator disk makes a stream tube outside which, the velocity remains undisturbed. The actuator disk theory relies on the following assumptions

- Steady and uniform flow upstream of the disk.
- Uniform and steady velocity at the disk.
- No rotation is imparted to the flow downstream of the disk.
- The flow passing through the disk is contained both upstream and downstream of the disk inside the stream tube.
- The flow is incompressible.

These assumptions are essentially in agreement with those of potential flow theory.

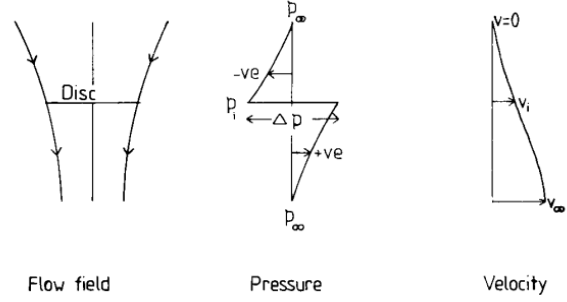


**Fig 3.a** The distribution of Flow field Pressure and Velocity through the actuator disk from far upstream to far downstream

The expression for induced velocity as given by momentum theory follows as

$$V_i = \sqrt{\frac{W}{2\rho A}} \quad (7)$$

Where  $A$  is the disk area,  $\rho$  is the density of flow and  $W$  is the total weight the rotor will carry which equals the thrust of vehicle in hover and steady forward flight. The rotor thrust can then be computed using

$$T = 2\rho A V_i^2 \quad (8)$$

And the induced power as

$$P_i = T V_i \quad (9)$$

### B. Blade Element Momentum Theory

Blade element momentum theory (BEMT) combines the results of momentum theory and classical blade element theory which divides the blade into a number of span-wise elements each of which follows the conservation principle for momentum and energy. This gives a better insight into the blade loading distribution. The inflow is no more uniform but it increases from root to tip. Blade element theory was coupled with Prandtl's tip and root loss factors and the empirical relations were also incorporated in a MATLAB code. The inflow ratio  $\tau$  (ratio of induced velocity to tip speed) is given by

$$\tau(r, \theta) = \sqrt{\left(\frac{\sigma C_{l\alpha}}{16}\right)^2 + \frac{\sigma C_{l\alpha}}{8} \theta r - \frac{\sigma C_{l\alpha}}{16}} \quad (10)$$

Here  $\theta$  is the pitch angle at the respective blade section,  $C_{l\alpha}$  is the lift curve slope,  $\sigma$  is the solidity factor defined as ratio of blades area by total disk area and  $r$  is the non-dimensional radial position of blade section.

For the validation of the BEMT code, its results were compared with those of experiment [6]. A rectangular blade section with NACA 0015 airfoil section was used in the experiment so the airfoil was first tested for its aerodynamic properties (lift curve slope and drag coefficient) in Xfoil. The drag term was then incorporated in the code using a 2<sup>nd</sup> order

polynomial expression as a function of angle of attack for higher accuracy.

TABLE 1 Test conditions used in BEMT code as in NACA report no. 626 [6]

Property	Value
Airfoil	NACA 0015
Chord length (m)	0.049
Reynolds number	242,000
Lift curve slope $C_{l\alpha}$	5.75
Rotational speed (rpm)	960
Blade span (m)	0.75
Root cutout length	0.125
Solidity factor	0.0424, 0.0636, 0.1060
Number of Blades	2,3,5
Number of Blade sections	100
$C_{D0}$	0.0098640
$C_{D1}$	-0.0001677
$C_{D2}$	0.0001954

The drag term used for profile power was determined using Xfoil results and a 2<sup>nd</sup> order polynomial curve fit was obtained in MATLAB as follows

$$C_D = C_{D0} + C_{D1} \cdot \alpha + C_{D2} \cdot \alpha^2 \quad (11)$$

C. Prandtl's Tip Loss Factor

To account for the loss of lift which takes place near the tips of blades because of finite number of blades, Prandtl's tip loss factor was incorporated in the BEMT code. The equation for the tip loss factor is written in terms of radial position  $r$ , number of blades  $Nb$  and inflow ratio  $\tau$  as shown in (12).

$$F = \frac{2}{\pi} \cos^{-1} e^{-\left(\frac{Nb}{2\tau}(1-r)\right)} \quad (12)$$

The modified form of (10) for inflow becomes

$$\tau(r, F, \theta) = \sqrt{\left(\frac{\sigma C_{l\alpha}}{16F}\right)^2 + \frac{\sigma C_{l\alpha}}{8F} \theta r} - \frac{\sigma C_{l\alpha}}{16F} \quad (13)$$

The dependency of inflow ratio on tip loss factor and tip loss factor on inflow ratio makes it difficult to calculate  $\tau$  directly at any radial section. To do this, an iterative numerical procedure was adopted, for which the results converged with fewer than 5 iterations each time.

D. Results

The code gives good results especially with small blade numbers. The reason for small discrepancies at higher values of solidity is because of the fact that with high number of blades, there are more wake interactions for each blade passing and results in a slightly lower value of thrust as compared to the results of BEMT. The error, however, is

never more than 5% and under 2% for maximum part of operation.

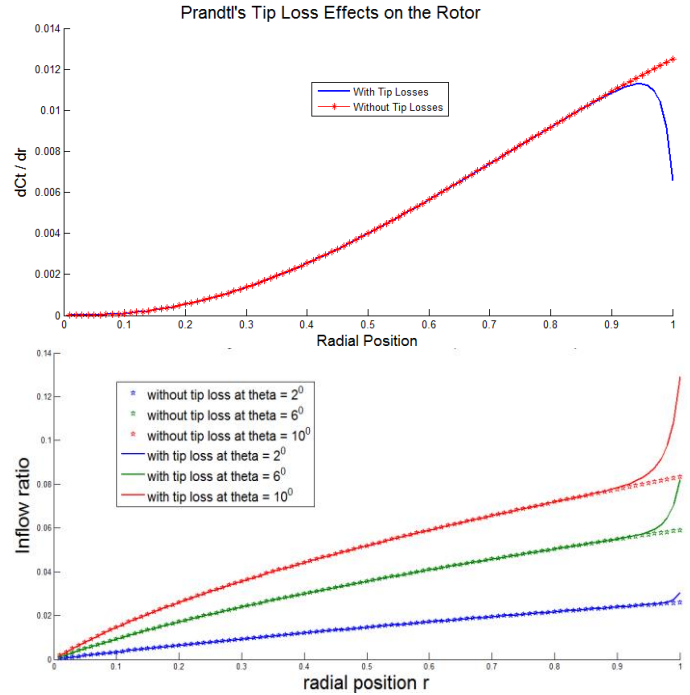


Fig 3.b Inflow Distribution along the radius of the blade with and without the tip losses as described by Prandtl

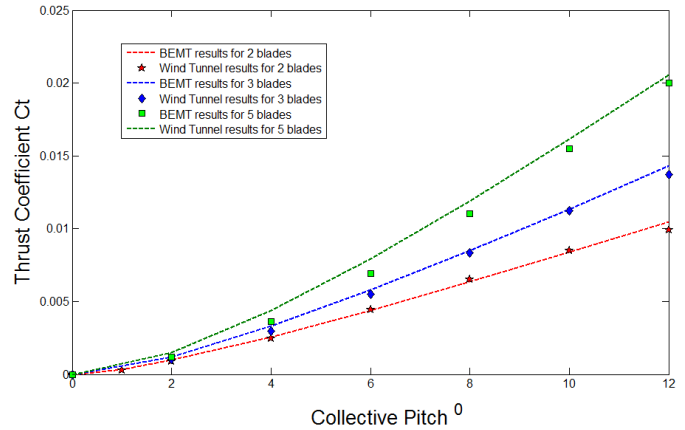
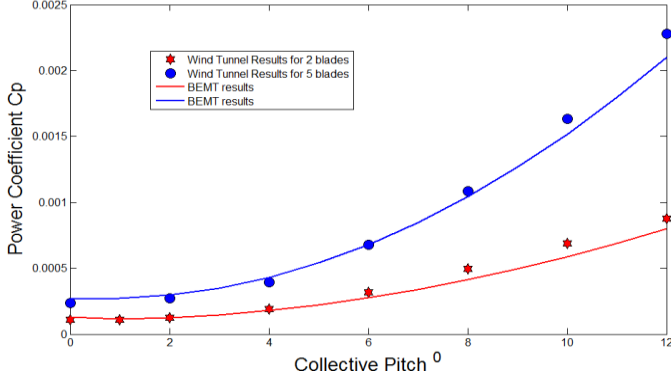


Fig 3.c BEMT code validation using experimental results [4] for thrust coefficient vs the collective pitch angle with 2,3 and 5 blades.

The power coefficient is over predicted by almost 20% if an average value of drag coefficient is used instead of 2<sup>nd</sup> order approximation which gives an accurate prediction of total power despite the fact that the blade hub adds on to the profile power, the effects of which have not been considered in BEMT code.



**Fig 3.d.** BEMT code validation using experimental results [4] for power coefficient vs. the collective pitch angle with 2 and 5 blades

#### IV. WAKE MODELING

For hovering flight, generalized prescribed wake models are often employed which allow for the prediction of inflow through the disk with lesser computation involved since these models rely on prescribing the location of rotor tip vortices as a function of wake age or time on the basis of experimental observations for hover flight. Landgrebe's model is one of the prescribed wake models based on the experimental findings made by Landgrebe for about seventy subscale helicopter configurations with varying number of blades, solidity, twist and aspect ratios. The following subsections describe how the position of tip vortex and the vortex sheet was determined using Landgrebe's model. The equations were employed in a MATLAB program coupled with the BEMT to accurately model the rotor wake.

##### A. Tip Vortex Position

Landgrebe describes the vertical position of tip vortex below the rotor disk as

$$\frac{z_{\text{tip}}}{R} = \begin{cases} k_1 \psi_w & \text{for } 0 \leq \psi_w \leq 2\pi/N_b \\ \left(\frac{z_{\text{tip}}}{R}\right)_{\psi_w=2\pi/N_b} + k_2 \left(\psi_w - \frac{2\pi}{N_b}\right) & \text{for } \psi_w \geq 2\pi/N_b \end{cases} \quad (14)$$

Here  $\psi_w$  describes the vortex age,  $R$  is the rotor radius,  $N_b$  is the number of blades,  $k_1$  and  $k_2$  are constants which are a function of rotor solidity, twist distribution and thrust coefficient and are given by

$$\begin{aligned} k_1 &= -0.25(C_T/\sigma + 0.001\theta_{tw}) \\ k_2 &= -(1 + 0.01\theta_{tw})\sqrt{C_T} \end{aligned} \quad (15)$$

The radial coordinates, in the Landgrebe's model are given by

$$\frac{y_{\text{tip}}}{R} = A + (1 - A) \exp(-\Lambda \psi_w) \quad (16)$$

The constants  $A$  also called the contraction ratio was set to 0.78 and  $\Lambda$  was determined using empirical relations as a function of thrust coefficient calculated by momentum theory.

##### B. Vortex Sheet

The inner parts of the blade shed vortices, trailing underneath the rotor domain in a form of a sheet, the position of which varies linearly along the blade span. The outer end of this vortex sheet at  $r=0$  is given as

$$\left(\frac{z}{R}\right)_{r=1} = \begin{cases} K_{1,r=1} \psi_w & \text{for } 0 \leq \psi_w \leq 2\pi/N_b \\ K_{1,r=1} \left(\frac{2\pi}{N_b}\right) + K_{2,r=1} \left(\psi_w - \frac{2\pi}{N_b}\right) & \text{for } \psi_w \geq 2\pi/N_b, \end{cases} \quad (17)$$

And the inner part as

$$\left(\frac{z}{R}\right)_{r=0} = \begin{cases} 0 & \text{for } 0 \leq \psi_w \leq 2\pi/N_b \\ K_{2,r=0} \left(\psi_w - \frac{\pi}{2}\right) & \text{for } \psi_w \geq \pi/2. \end{cases} \quad (18)$$

The variables  $N_b$  and  $\psi_w$  have already been defined. The position of the vortex sheet at the inner parts of the blade was determined by linearly interpolating between the root and the tip. The coefficients  $K_1$  and  $K_2$  for the sheet coordinates at  $r=0$  and  $r=1$ , were determined using empirical relations as a function of thrust coefficient and twist rate which was set to zero in our case since no twist case is being considered for simplicity.

##### C. Results

The wake was modelled for a 2 bladed rotor system. The blade collective pitch was set to 10 degrees. The airfoil data was imported for NACA 0015 section used previously for BEMT validation.

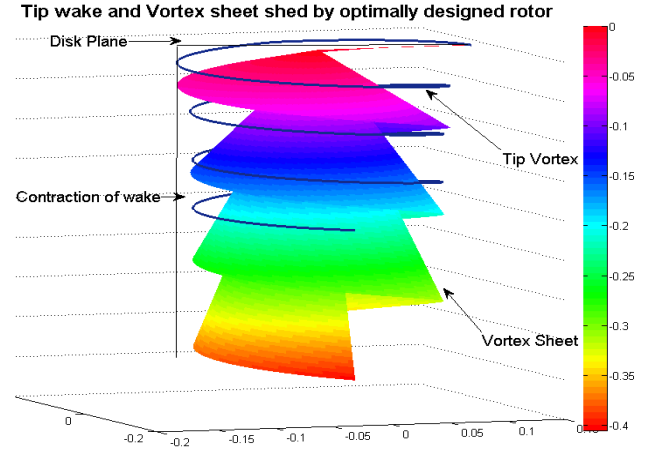


**Fig 4.** Position of tip vortex and the vortex sheet as a function of blade azimuth and radial location, using Landgrebe's model below the rotor disk plane

#### V. FORWARD FLIGHT INFLOW DISTRIBUTION

In forward flight, the rotor provides the lifting force as well as the propulsive force for forward motion which overcomes the rotor and airframe drag. As the rotor is no longer hovering, it progresses forward because of which a part of the blade which is advancing towards the flight direction, experiences higher velocity while the other part which is retreating

experiences lower velocity. All blade components experience a component of the free stream velocity  $V_\infty$  as in (2).

It is important to define some basic terms as used in forward flight.

1. Advance Ratio ( $\mu$ ): This is the non-dimensional forward flight speed defined as the ratio of forward speed to the blade tip speed.

$$\mu = \frac{V_\infty}{\omega R} \quad (19)$$

2. Blade Azimuth ( $\psi$ ): This is defined as the angle between the blade section and the reference axis. This describes the position of the blade in the rotor disk plane.
3. Wake Skew Angle ( $\chi$ ): This is the angle as shown in figure 5.a that the rotor wake makes with the rotational axis. At advance ratios greater than 0.2, this angle is found to be more than 75 degrees.

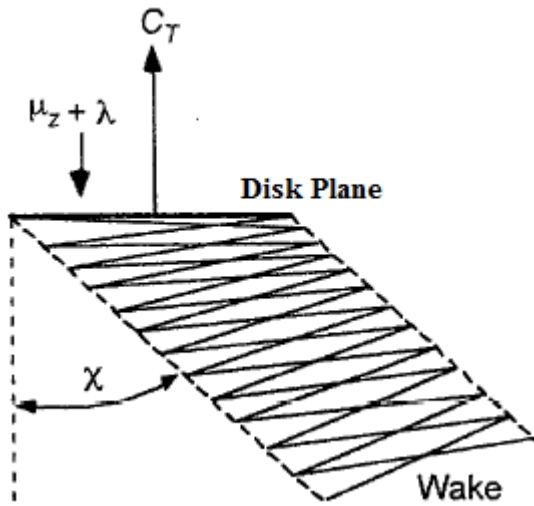


Fig 5.a Skewed wake description as a result of forward flight velocity [4]

The periodic variation in the local velocity gives rise to a number of aerodynamic complications such as blade flapping, compressibility effects, nonlinear aerodynamics, stall and complex induced velocity distribution. The application of blade element theory requires an estimate of the induced velocity at each blade section to determine thrust and power coefficients. The induced velocity is no more axi-symmetric as in case of hover. The induced velocity in forward flight is given by various inflow models which can be classified overall as

1. Linear Inflow models.
2. Non-linear Inflow models.

## VI. LINEAR INFLOW MODELS

The longitudinal and lateral inflow distribution is assumed to vary linearly in these models. These models are based on the findings of Brotherhood and Stewart (1949) and Bramwell (1976), Heysona and Katsoff(1957). Brotherhood performed

an experiment in which smoke streamers were placed upstream of the rotor and their angular displacement was used to determine the inflow pattern. The results suggested linear variation in the longitudinal inflow.

Experimental findings suggest that while there is a transition from hover to forward flight i.e.  $0 < \mu < 0.1$ , inflow is most non uniform. At advance ratios higher than 0.15, inflow becomes more linear and can be approximated using

$$\lambda = \lambda_0 \left( 1 + k_x \frac{x}{R} + k_y \frac{y}{R} \right) \quad (20)$$

Here  $\lambda_0$  is given by momentum theory results

$$\lambda_0 = \frac{C_T}{2\sqrt{\mu^2 + \lambda^2}} \quad (21)$$

The coefficients  $k_x$  and  $k_y$  are the longitudinal and lateral inflow coefficients given by empirical relations. The equations are solved iteratively.

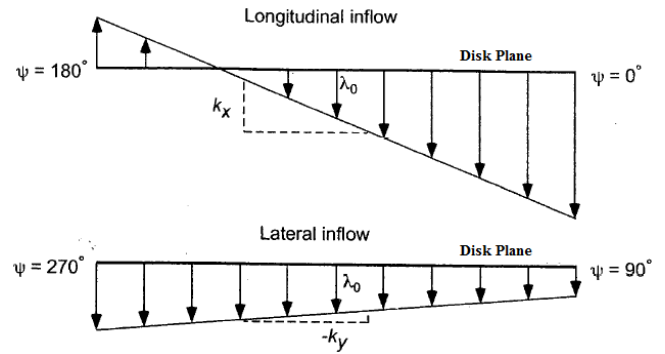


Fig 5.b Linear Inflow model approximating longitudinal and lateral flow [4]

### A. Drees' Model

Drees model is a linear inflow model which considers a sinusoidal loading considering trailing edge vortex and shedding vortex. Drees model is essentially based on actuator disk approach. The predicted inflow is a function of position and stays constant with time for a fixed position or azimuth. The variables  $k_x$  and  $k_y$  in the linear inflow equation are given by

$$k_x = \frac{4}{3} \left( \frac{1 - \cos \chi - 1.8 \mu^2}{\sin \chi} \right) \quad (22)$$

$$k_y = -2\mu$$

Here  $\chi$  is the wake skew angle and  $\mu$  is the advance ratio. Fig. 5c relates the results of linear inflow model of Drees with those of experiment. The experimental data has been taken from the NASA technical memorandum which uses LASER velocimeter for inflow measurements. The variation in the curvature near the root  $r=0$  at all azimuth angles can be regarded to the hub losses in actual experiment.

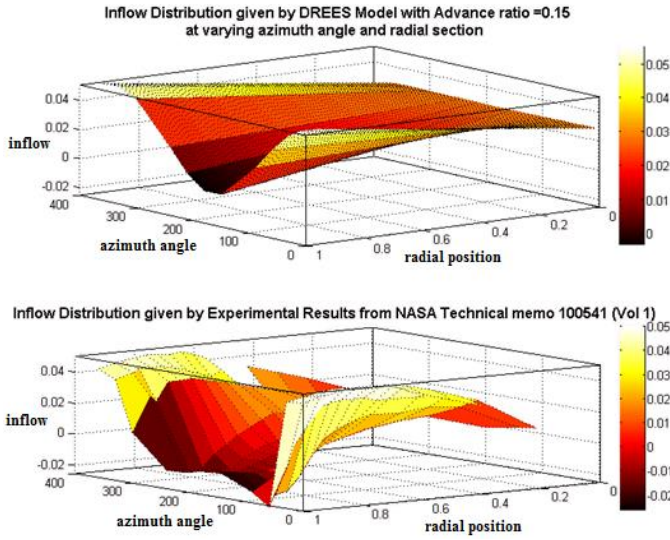


**Fig 5.c** Comparison between the inflow as suggested by Drees model and experiment. Inflow

### B. Payne's Model

Payne's model also suggests loading similar to that of Drees. It suggest a linear inflow independent of lateral variations. Payne's model is based on the numerical results from experiments. The longitudinal inflow coefficient is given by

$$k_x = \frac{4}{3} \left( \frac{\frac{\mu}{\chi}}{1.2 + \frac{\mu}{\chi}} \right) \quad k_y = 0 \quad (23)$$

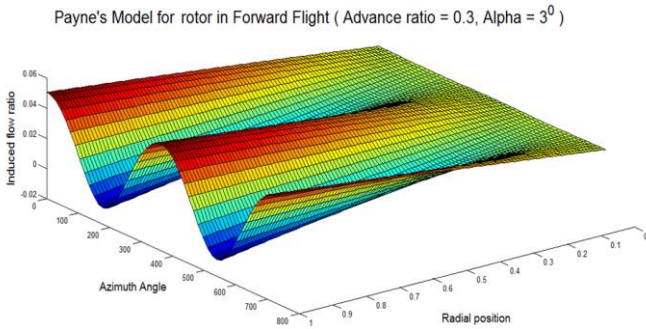


**Fig 5.d** Inflow distribution as suggested by Payne's model as a function of radial position and azimuth angle

As seen in Fig. 5d the inflow rises along the blade span from  $r=0$  to  $r=1$  at  $0$  azimuth angle. On the advancing side of the blade at  $90^\circ$  azimuth angle the inflow rises more slowly as compared to  $0$  azimuth angle. At  $180^\circ$  azimuth position, the inflow is seen to be negative which suggest that there is an upwash instead.

### C. Pit and Peter's (PnP) Model

This model was suggested almost 36 years later after Drees. PnP model is again similar to Payne's model which suggests inflow distribution independent of lateral variations. The longitudinal coefficient is given by

$$k_x = \frac{15\pi}{23} \tan \frac{\chi}{2} \quad (24)$$

The inflow coefficient is independent of the advance ratio in this model. In Drees model, the longitudinal inflow coefficient was inversely related to the advance ratio i.e. at higher advance ratios, the inflow variation from at  $0$  azimuth and  $180$  azimuth is more relaxed.

Pit and Peter's Model suggesting Inflow Distribution (Advance ratio = 0.3, Alpha = 3)

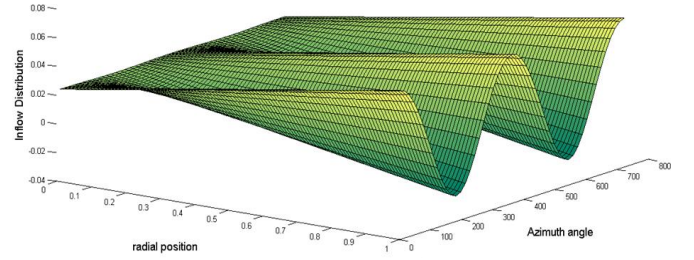


**Fig 5.d** Inflow distribution as suggested by Payne's model as a function of radial position and azimuth angle

## VII. NON LINEAR INFLOW MODELLING

### A. Mangler and Squire's (MnS) Model

Mangler and Squire's model is a nonlinear inflow model based on incompressible, linearized, Euler equations. The solutions of this model satisfy the conditions for potential flow and the laplace equation is satisfied. The effects of different forms of loading may now be combined by superposition. The model suggests two loading types. Type-I loading is elliptic and Type-III loading which vanishes near the edges and centres of the disk.

The resulting inflow is described by the Fourier series as follows

$$\lambda_i = \left( \frac{2C_T}{\mu} \right) \left[ \frac{c_0}{2} + \sum_{n=1}^{\infty} (-1)^n c_n(r, \alpha) \cos n\psi \right] \quad (25)$$

For Type-I loading, the coefficients are given by

$$c_0 = \frac{3}{4}v \quad \text{and} \quad c_1 = -\frac{3\pi}{16} \sqrt{1-v^2} \left( \frac{1-\sin\alpha}{1+\sin\alpha} \right)^{1/2} \quad (26)$$

For even values  $n > 2$

$$c_n = (-1)^{\frac{n-2}{2}} \left( \frac{3}{4} \right) \left( \frac{v+n}{n^2-1} \right) \left( \frac{1-v}{1+v} \right)^{\frac{n}{2}} \left( \frac{1-\sin\alpha}{1+\sin\alpha} \right)^{\frac{n}{2}} \quad (27)$$

And for odd values,  $n > 2$ ,  $c_n = 0$ . Here  $v = \sqrt{1-r^2}$ . The elliptic loading is shown in Fig. 7a. A higher inflow is seen near the far end of the disk at  $0^\circ$  azimuth position whereas an upwash is seen on the advancing end of the disk at  $180^\circ$  azimuth angle.

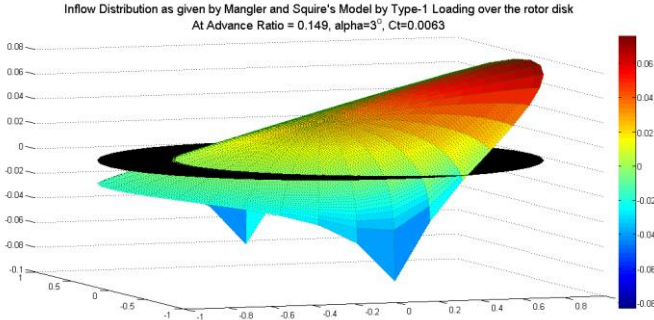


**Fig 7.a** Inflow distribution as suggested by Type-I loading in MnS model over the actuator disk.

For Type-III loading, the coefficients are given by

$$\begin{aligned} c_0 &= \frac{15}{8}v(1 - v^2), \\ c_1 &= -\frac{15\pi}{256}(5 - 9v^2)\sqrt{1 - v^2} \left( \frac{1 - \sin \alpha}{1 + \sin \alpha} \right)^{1/2} \\ c_3 &= \frac{45\pi}{256}(1 - v^2)^{3/2} \left( \frac{1 - \sin \alpha}{1 + \sin \alpha} \right)^{3/2}. \end{aligned} \quad (28)$$

For odd values  $n > 4$ ,  $c_n = 0$  and for even values  $n > 1$

$$\begin{aligned} c_n &= (-1)^{\frac{n-2}{2}} \left( \frac{15}{8} \right) \left[ \left( \frac{v+n}{n^2-1} \right) \left( \frac{9v^2+n^2-6}{n^2-9} \right) + \left( \frac{3v}{n^2-9} \right) \right] \\ &\times \left( \frac{1-v}{1+v} \right)^{\frac{n}{2}} \left( \frac{1-\sin \alpha}{1+\sin \alpha} \right)^{\frac{n}{2}} \end{aligned} \quad (29)$$

Fig.7b shows how Type-III loading suggests loading on the disk. It can be seen that the inflow is more dominant in between the root and tip sections and it vanishes at the centre of disk.

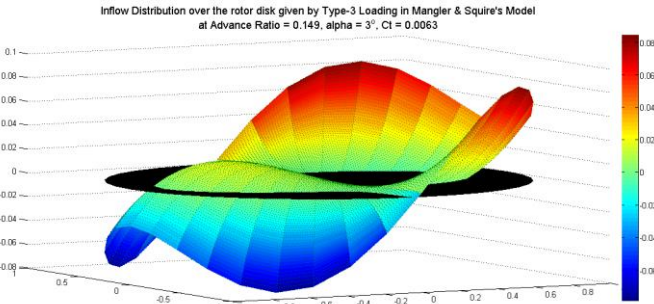


**Fig 7.b** Inflow distribution as suggested by Type-III loading in MnS model over the actuator disk.

## VIII. RESULTS AND CONCLUSION

The results of various inflow models in forward flight were compared with those of experimental results from NASA technical memorandum [5]. The experimental results were converted to a circular grid and plotted in MATLAB using

surf command. The following figure relates the results of various theories in forward flight for inflow distribution. In the experiments performed, the presence of hub at the centre of the disk causes a higher inflow velocity than suggested by various models.

The uniform inflow as suggested by actuator disk approach coupled with momentum theory provides least accurate results in forward flight. The Drees model as shown by a line of negative gradient, is successful in predicting the general trend of pressure loading and also the inflow but it fails to capture the flow behaviour on the outer ends of the disk. MnS model provides a far better picture of inflow as compared with that of Drees model. On the outer ends of the disk, the MnS model provides most accurate prediction.

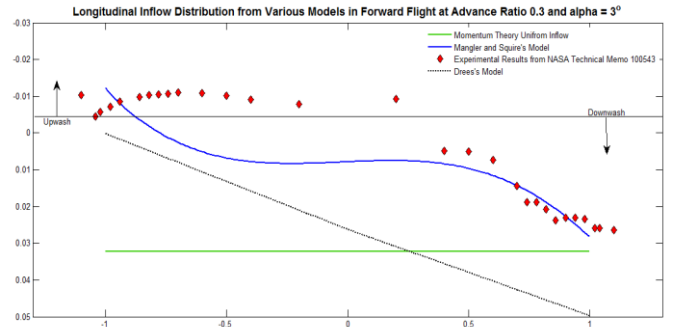


**Fig 8** Validation of inflow modelling results in forward flight

The results of each model are compared with the experimental results for verification. BEMT gives most accurate prediction of inflow distribution in hover while MNS model gives best results in forward flight.

## IX. ACKNOWLEDGMENT

I would like to thank my supervisor Dr. Khalid Pervez and above all my parents in supporting me both morally and technically throughout the research work.

## X. REFERENCES

- [1] J. Seddon, "Basic Helicopter Aerodynamics", 1990, ISBN 0-632-02032-6
- [2] "Inflow measurements made with LASER velocimeter – Vol 1", *NASA Technical Memorandum 100541*, April 1998
- [3] J. Gordon Leishman, "Principles of helicopter aerodynamics", 2<sup>nd</sup> edition, ISBN 0-521-66060-2
- [4] M. Knight, R. A. Hefner, "Static thrust analysis of the lifting airscrew", *602 NACA Technical notes*
- [5] Robert T. N. Chen, "A survey of non-uniform inflow models for rotorcraft flight dynamics and control applications", *NASA Technical Memorandum 102219*, November 1989
- [6] T. W. Streett, "Rotor design for an unmanned helicopter for use on Mars"
- [7] Ngoc Anh Vu a.b. Jae Woo Lee b, Jung Il Shu, "Aerodynamic design optimization of helicopter rotor blades including airfoil shape for hover performance", *Chinese Journal of Aeronautics*, 2013